

Pulse-picking coherent anti-Stokes Raman scattering microscopy for highly sensitive chemical imaging

Matthew Clark

Purdue University

Gil Gonzalez

Purdue University

Chi Zhang (✉ zhan2017@purdue.edu)

Purdue University

Article

Keywords: coherent anti-Stokes Raman scattering, pulse-picking technology, acousto-optic modulator, multiphoton fluorescence, second harmonic generation modalities

Posted Date: September 28th, 2021

DOI: <https://doi.org/10.21203/rs.3.rs-846172/v1>

License: © ⓘ This work is licensed under a Creative Commons Attribution 4.0 International License. [Read Full License](#)

Abstract

Coherent Raman scattering has been developed into powerful technologies for the chemical imaging of biological samples. However, limited sensitivity remains a critical bottleneck for coherent Raman microscopes. We introduce a pulse-picking technology that can significantly increase the sensitivity of coherent anti-Stokes Raman scattering (CARS) microscopy. An acousto-optic modulator driven by a function generator allows picking collinearly combined pump and Stokes pulses at low duty cycles. This method reduces the number of pulses at each image pixel, enhances the peak power of laser pulses, and thus significantly improves the sensitivity of CARS and minimizes phototoxicity. We demonstrated an over 1000-fold sensitivity improvement for CARS imaging. Besides, we show this pulse-picking method can enhance the sensitivity of multiphoton fluorescence and second harmonic generation modalities about 20 times. Using cell and biological tissue samples, we highlight the potential of this pulse-picking technology for highly sensitive multimodal chemical imaging in biological and medical sciences.

Introduction

Chemical analysis of biological samples is the key to understanding biofunctions and diagnosing disease transitions. There is a growing interest in the label-free acquisition of chemical information in living samples. Coherent Raman scattering (CRS) processes, including both the coherent anti-Stokes Raman scattering (CARS) and stimulated Raman scattering (SRS), harness molecular vibrational transitions excited by ultrafast laser pulses for chemical analysis [1–4]. CRS signals offer chemical information beyond fluorescence and minimize perturbation to biological systems. Continuous technology advancements and growing applications of CRS microscopy in the past two decades have transitioned CRS into powerful platforms for biological and medical research [5–14].

Although CRS signals can be a million times stronger than spontaneous Raman scattering signals, they are still orders of magnitudes weaker than fluorescence signals. The quest for better sensitivity emerges at the inception of the technology and still prevails today as one of the most attractive pursuits of CRS imaging. Multiple approaches have been utilized to improve the sensitivity of CRS microscopy. One way is to enhance signals by metal surfaces or nanoparticles. Using patterned gold surfaces, the enhancement of CARS signals can reach $\sim 10^5$ times [15]. By placing a molecule between a dipolar nano-antenna, CARS was shown to detect single molecules [16]. Surface enhancement can also boost SRS sensitivity similar to conventional surface-enhanced Raman scattering [17] and the sensitivity can also reach the single-molecule level [18]. Another commonly used method is by designing unique Raman tags that work in electronic pre-resonance conditions for imaging. Efforts from multiple groups have pushed pre-resonance SRS imaging to a sensitivity of micro- to nanomolar [19–21]. As well, coupling SRS with fluorescence can also give superb sensitivity for specially designed molecules [22, 23].

Although these methods offer strong CRS signal enhancement even to single molecule-level detection, they require either specially designed Raman tags or metal surfaces. Another path to generally improve both sensitivity and resolution of CRS microscopy is to use shorter wavelengths for excitation [24]. Shorter excitation wavelengths in the visible range have stronger scattering and may induce electronic pre-resonance. Visible beam excitations were shown to improve the sensitivity of SRS ~ 23 times, however, at the costs of lowering the

threshold of photodamage of biological specimens and increasing system complexity. Besides, denoising methods were also developed by multiple groups through total variation minimization [25] and deep learning [26–28]. Nonetheless, the denoising methods may introduce artifacts and computational complexity, or require a large data set for training.

We develop a pulse-picking technology that can be generally applied to any form of CARS, multiphoton excitation fluorescence, and harmonic generation microscopy modalities for highly sensitive label-free chemical imaging. Using an acousto-optic modulator (AOM) controlled by a function generator, we can reduce the duty cycle of high repetition rate laser pulses and greatly enhance the pulse peak power. Applying one of the laser beams at Bragg angle error condition, the pump and Stokes beams at the 1st order of the AOM can be collinearly combined. We demonstrate over 1000 times improvement of sensitivity for CARS and about 20 times for degenerate two-photon excitation fluorescence (TPEF) and second harmonic generation (SHG). These sensitivity enhancements allow us to generate strong TPEF and SHG signals with picosecond laser pulses, meanwhile, optimize spectral resolution for hyperspectral CARS microscopy and minimize phototoxicity to biological samples. This technology is widely applicable to nonlinear optical microscopes and would expand the applications of label-free chemical imaging in biological and medical sciences towards better sensitivity and low perturbation.

Results

Design of the pulse-picking nonlinear optical microscope

Up to date, the most widely used light sources for nonlinear optical microscopy are high-repetition-rate femtosecond or picosecond lasers. Assuming an 80 MHz laser repetition rate and a 10 μ s pixel dwell time, there are 800 pulses on each image pixel. Since nonlinear optical signals are usually proportional to the square or cubic of laser peak power, reducing the number of pulses at each pixel with higher pulse energy can largely improve the sensitivity while maintaining the same average input power. We develop a pulse-picking technology to reduce the duty cycle of high repetition rate lasers for high sensitivity nonlinear optical microscopy. The design of our microscope is illustrated in Fig. 1a. We use a femtosecond laser with synchronized dual outputs: one as the Stokes beam with a fixed wavelength at 1045 nm and the other as the pump beam with a tunable wavelength from 690–1300 nm. The two beams are combined and chirped by multiple SF-57 glass rods for spectral focusing. Before the microscope, the Stokes pulse is chirped to 1.8 ps while the pump pulse is chirped to 3.4 ps. The ratio of pulse durations matches the ratio of spectral widths to ensure the best spectral resolution using spectral focusing [29]. The combined beams are sent to an acousto-optic modulator (AOM) that is controlled by a function generator. Square waves with tunable duty cycles from 1.4–97% at various modulation frequencies are sent to the AOM for pulse picking. We direct the 1st order AOM output to a lab-designed upright laser-scanning microscope with two photomultiplier tubes (PMTs) in the epi-direction and one in the forward direction. As shown in Fig. 1a, we use PMT1 for forward CARS (FCARS) detection, PMT2 for the acquisition of TPEF signals at 450 nm, and PMT3 for collection of either TPEF signals at 570 nm, or SHG signals, or epi CARS (ECARS) signals.

We choose the 1st diffraction order from the AOM over the 0th order for imaging because it will completely shut off the laser beam at the ‘time-off’ periods. This maximizes the nonlinear optical signal generation at a fixed

input average power. However, the AOM Bragg angles for the pump and Stokes wavelengths are different. To ensure beam overlap along the 1st order of diffraction, one of the beams needs to be slightly misaligned from the perfect Bragg angle. The AOM beam separation angle between the 0th and 1st orders, regardless of the incidence angle, is

$$\theta_s = \frac{\lambda f}{V}$$

1

where λ is the beam wavelength, f is the acoustic frequency, and V is the acoustic velocity. The Bragg angle is half of the separation angle

$$\theta_B = \frac{\lambda f}{2V}$$

2

The laser beam geometry at the AOM for spatially overlapping pump and Stokes beams along the 1st order diffraction is illustrated in Fig. 1b. We first let the pump beam at 800 nm enter the AOM at the Bragg angle θ_B . Both the 0th and the 1st diffraction orders of this wavelength have an angle of θ_B to the crystal surface normal. Assuming the Stokes beam at 1045 nm has a Bragg angle $\theta'_B = \theta_B + \theta'$, the incidence angle of this beam needs to be slightly detuned from θ'_B to generate the 1st order diffraction at the same direction of the 1st order pump beam. If δ is the angle between the incidence angle and the Bragg angle of the Stokes beam, it satisfies

$$\theta_{s,\text{Stokes}} = 2(\theta_B + \theta') = 2\theta_B + \theta' + \delta$$

3

This gives $\delta = \theta'$,

and indicates that when the pump and Stokes beams are collinear at the 1st order of pump, the angle between the incidence and the Bragg angle of the Stokes beam equals the angle difference between the pump and Stokes Bragg angles. In our optical configuration, $\delta=0.46^\circ$. Using two mirrors in the Stokes-only beam path, we can fine-tune the incidence angle of the Stokes beam at the AOM to satisfy this condition. Using this method, we can reach a 60% efficiency for the pump and 42% efficiency for the Stokes beam using a 90% duty cycle. The loss of efficiency is due to the suboptimal crystal anti-reflective coating and Bragg angle errors.

Pulse-picking for sensitivity improvement

Laser pulses from both the pump and Stokes beams picked by the AOM at different duty cycle values are displayed in Fig. 1c. We estimate the rise time of the AOM in our experiment is ~ 23 ns for the Stokes and ~ 17 ns for the pump (Supplementary Information 1), slightly longer than the time interval between adjacent pulses from the laser, which can also be inferred from Fig. 1c. At high duty cycles, the number of pulses picked by the AOM is proportional to the duty cycle. At 5% duty cycle, we were able to pick 4 major pulses for both pump and

Stokes beams at 1.1 MHz modulation frequency. When the duty cycle is reduced to 2% or below, as few as one major pulse can be picked.

Reducing the laser duty cycle would enhance the sensitivity of CARS microscopy at the same input average power. The intensity of the CARS signal can be expressed as

$$I_{CARS} \propto \left| \chi^{(3)} \right|^2 I_p^2 I_s$$

4

where I_{CARS} , I_p and I_s are, respectively, the intensities of the CARS, pump, and Stokes beams. $\chi^{(3)}$ is the third-order nonlinear optical susceptibility. The intensity of a laser pulse can be expressed as

$$I = \frac{E}{\tau A} = \frac{P}{f\tau A}$$

5

Here, E , τ , and A are pulse energy, pulse width, and laser focus area of the laser beam, while P and f are the laser average power and repetition rate, respectively. By modulating combined laser beams at a lower frequency and applying a duty cycle of D , we have

$$P_{CARS} = fD\tau_{CARS}A \cdot I_{CARS} = fD\tau_{CARS}A \cdot \left| \chi^{(3)} \right|^2 \left(\frac{P_p}{fD\tau_p A} \right)^2 \frac{P_s}{fD\tau_s A} = \left| \chi^{(3)} \right|^2 \frac{P_p^2 P_s}{f^2 D^2 A^2} \frac{\tau_{CARS}}{\tau_p^2 \tau_s} \propto \frac{1}{D^2}$$

6

This indicates the pulse picking CARS (PPCARS) average signal is reciprocal to the square of the duty cycle. Similarly, we can derive that for the TPEF and SHG processes, the average signal is proportional to the reciprocal of D .

$$P_{TPEF}, P_{SHG} \propto \frac{1}{D}$$

7

Chemical imaging by the pulse-picking nonlinear optical microscope

Figure 1d shows the relationship between the sensitivity enhancement and duty cycle for FCARS signals at different modulation frequencies. We used the dimethyl sulfoxide (DMSO) CH_3 symmetric stretching peak at 2915 cm^{-1} for the signal-to-noise ratio (SNR) analysis. A boundary of a DMSO drop sandwiched between two glass coverslips was imaged for SNR calculation. We measured the SNR of the DMSO by dividing the average value of the DMSO signal by the standard deviation of the empty area. For each duty cycle measured in Fig. 1d, the SNR was divided by the SNR of the 97% duty cycle to calculate the sensitivity increase. A $1/D^2$ curve is plotted as a reference. We find that the experimental data matches the theoretical curve very well at high duty

cycles but starts to deviate from the theory at very low duty cycles. The maximum sensitivity enhancement we were able to obtain is 1078 at 1.4% duty cycle, 700 kHz. The major cause of sensitivity drop at very low duty cycles might be the unlocked phase between the function generator modulation and the laser pulse train. Frequency drifts between the two are less significant when the duty cycle is high since almost the same number of pulses can always be picked at any phase difference. However, when the duty cycle becomes low, especially below 4%, the phase drifts can greatly impact the number of pulses picked by the AOM. Figure 1e displays correlations between modulation frequency and SNR increase at different duty cycles. These results show that at high duty cycles (> 20%), the SNR increase is very similar at different modulation frequencies, while at low duty cycles (< 20%), lower modulation frequency gives stronger SNR. The SNR decrease at 300 kHz is likely due to the drift between modulation and acquisition of image pixels.

We used fluorescent polystyrene beads and measured the fluorescence signal at 450 nm excited by 800 nm laser pulses (Fig. 1f) to evaluate the sensitivity enhancement of TPEF, which shows a near 1/D relation at high duty cycles and starts to deviate from the theoretical curve at lower duty cycles. We can obtain a 16.3 sensitivity increase at a 2% duty cycle, 700 kHz. SHG signal improvement, which shows a similar dependence as the TPEF, was measured using a mouse tail tendon specimen and 1045/522 nm excitation/detection (Fig. 1g). A sensitivity increase of 14.5 was achieved at a 2% duty cycle, 1.1 MHz. Plots of TPEF/SHG SNR improvement versus duty cycle at other modulation frequencies are plotted in Figure S2, showing the maximum sensitivity enhancement of ~ 20 folds for both TPEF and SHG.

To measure the absolute sensitivity of our microscope, we performed hyperspectral CARS imaging. A spectral phase retrieval method based on Kramers–Kronig relations was used to derive Raman spectra from chemical compounds using FCARS spectra [30–32]. Figure 2a shows CARS spectra of DMSO and methanol in the C-H stretching region. We measured the sensitivity of the PPCARS system using the 2915 cm^{-1} peak of DMSO diluted in D_2O . The retrieved CARS signal intensity versus DMSO concentration is shown in Fig. 2b, from which a quadratic relationship, which agrees with Eq. 4, can be identified. Retrieved Raman spectra of DMSO below 1% concentration are shown in Fig. 2c. SNR calculations (Supplementary Information 4) indicate that the lowest concentration detectable using 1.1 MHz modulation is 0.1%, corresponding to 14.2 mM DMSO. To detect such a concentration, only 5.2 mW pump and 6.2 mW Stokes were used at the sample. Using 700 kHz modulation, we can detect 0.05% DMSO, equaling to 7.1 mM concentration using only 2.0 mW pump and 3.7 mW Stokes beams at the sample (Figure S3). By fitting the 2915 cm^{-1} DMSO peak using a Lorentzian function, as shown in Fig. 2e, we measured the spectral resolution of our system to be 16.1 cm^{-1} in the C-H region.

Figure 2e plots retrieved Raman spectra of polystyrene (PS) and polymethyl methacrylate (PMMA) in the $1570\text{--}1750\text{ cm}^{-1}$ Raman fingerprint region acquired using $1\text{ }\mu\text{m}$ PMMA and PS mixed particles. The PS peaks at 1583 cm^{-1} (C = C stretching) and 1602 cm^{-1} (ring-skeletal stretching) can be resolved, while the PMMA peak at 1736 cm^{-1} is also detected. Using the strong peak at 1602 cm^{-1} , we measured a 9.1 cm^{-1} CARS spectral resolution of our microscope in this region. Figure 2g compares CARS images of mixed PMMA and PS beads at $\sim 1602\text{ cm}^{-1}$ using 97% and 4% duty cycles. A clear SNR and contrast improvement can be seen at the reduced duty cycle. By spectral phasor analysis of hyperspectral CARS images in the fingerprint region, we can separate PMMA and PS microparticles, as shown in Fig. 2h. For all the fingerprint imaging, 13.7 mW pump and 6.2 mW Stokes beams were used at the sample with a $10\text{ }\mu\text{s}$ pixel dwell time.

Cell imaging by the pulse-picking nonlinear optical microscope

Next, we applied PPCARS for cell imaging. Fig. 3a compares single-colour FCARS (top) and ECARS (bottom) images from Mia PaCa-2 cells at different duty cycles. We used 700 kHz modulation frequency and observed a continuous increase in signal and sensitivity for both FCARS and ECARS as the duty cycle decreased from 97% to 1.4%. To better compare the sensitivity improvement, we plot the intensity profiles along the lines in Fig. 3a (see Fig. 3b), which show a signal improvement of $\sim 250\times$ at the 1.4% duty cycle. We note that the sensitivity enhancement for small lipid droplets in the cells is less than the pure samples shown in Fig. 1. This is due to the higher ratio of nonresonant contribution at laser focus. Power at the sample for imaging is 10.8 mW for the pump and 5.0 mW for the Stokes. Cell imaging results using different duty cycles at 1.1 MHz modulation frequency are shown in Figure S4. We have also performed live-cell imaging of lipid droplets and mitochondria using CARS and TPEF signals from a mitochondria marker. Images comparing 97%, 10%, and 4% duty cycles are shown in Figure S5.

Hyperspectral CARS images of cells were performed using 2.0 mW pump and 3.7 mW Stokes excitation power at 10 μs pixel dwell time. By spectral focusing and spectral phasor unmixing, we can separate major cellular compositions including cytosol, endoplasmic reticulum, nuclei, and lipid droplets in cells using both FCARS (Fig. 3c) and ECARS (Figure S6) images. The composited chemical map of cells and retrieved Raman spectra of four major components using FCARS are shown in Figs. 3d and 3e, respectively. The separation capability of our hyperspectral CARS microscopy is comparable to spectral-focusing-based hyperspectral SRS [29, 33]. We also performed 3D imaging of a Mia PaCa-2 cell as shown in Fig S7 and Supplementary video 1, demonstrating the 3D chemical imaging capability of the PPCARS microscope.

Tissue imaging by the pulse-picking nonlinear optical microscope

To evaluate sensitivity enhancement of our multimodal microscope for tissue imaging, we compared FCARS, ECARS, TPEF at 450 nm, and TPEF at 570 nm images of mouse liver tissue at 97% and 4% duty cycles under 1.1 MHz modulation (Figs. 4a-d). CARS excitation wavelengths are tuned to the CH_2 stretching at 2855 cm^{-1} . Signals in the TPEF 450 nm channel are majorly contributed by the autofluorescence from nicotinamide adenine dinucleotide (NADH) while in the TPEF 570 nm channel are contributed by the autofluorescence from flavin adenine dinucleotide (FAD). To better compare the contrast enhancement, we combine two duty cycle images into one and display half of each. We also select a smaller field of view and show a magnified image on the right of each large area image. Intensity profiles along the lines in Figs. 4a-d are plotted in Fig. 4e. These results show strong SNR enhancement for all modalities at 4% duty cycle. We also display ECARS mouse kidney tissue images at 97% and 10% duty cycle to demonstrate sensitivity increase at a moderate duty cycle (Fig. 4f). As well, we show sensitivity enhancement of SHG imaging using mouse tail tendon in Fig. 4g. Images from other tissue samples and at other modulation frequency/duty cycles can be found in the Supplementary Information (Figure S8-12). These results highlight the potential of pulse-picking technology for the chemical analysis of intact biopsy samples for diagnostics.

Discussion

In this work, we developed a pulse-picking technology to increase the sensitivity of multiple nonlinear optical imaging modalities including CARS, TPEF, and SHG. Using function-generator-controlled AOM and applying one of the excitation beams at a Bragg angle error condition, we collinearly combined both pump and Stokes beams at the 1st order of AOM. By reducing the duty cycle of the laser beams, we could improve the SNR or CARS imaging up to 1078 times for pure samples. This method also offers about 20 times sensitivity enhancement for TPEF and SHG. With 10 μ s pixel dwell time, hyperspectral PPCARS can detect 7 mM DMSO in deuterated oxide with less than 6 mW total excitation power on the sample. The low excitation power and short pixel dwell time used in this work minimize the phototoxicity of lasers for nonlinear optical imaging.

Above the 10% duty cycle, the sensitivity enhancements for all nonlinear optical processes match theoretical predictions. Below 10%, deviations start to increase between the experimental results and the theoretical curve. The optimal duty cycle varies at different modulation frequencies, while the optimal modulation frequency is dependent on the pixel dwell time. The best duty cycle value decreases at lower modulation frequencies. The decrease in sensitivity improvement for CARS at very low duty cycles is likely due to the pulse-picking variations and drifts caused by the unlocked phase between the laser repetition frequency and the modulation frequency, as well as the rise time difference between pump and Stokes pulses. These variations only exist at the rise and fall time of each cycle, and thus are not significant for high duty cycles. However, at very low duty cycles, since only a few pulses are picked, large deviations can be induced. Lower modulation frequencies would further improve the sensitivity at lower duty cycles, however, might limit the imaging speed. To avoid intensity drifts between different pixels, at low modulation frequencies, pixel dwell time might need to be carefully selected. Besides, we expect that phase-locking the function generator to the laser repetition would further improve the sensitivity values at low duty cycles.

The performance of PPCARS microscopes can be further improved in several ways. First, the lowest duty cycle we can achieve is 1% using 700 kHz and 300 kHz modulation frequency. Further reducing the duty cycle would continue to boost the sensitivity at low modulation frequencies. Second, the efficiency of the AOM can be further improved using optimized crystal coating. Third, using an electro-optic modulator, which has a higher rise time and does not shift angles at different wavelengths, might give better sensitivity enhancement at low duty cycles.

Typically, TPEF and SHG biological imaging prefer fs lasers for excitation [34, 35]. With significant sensitivity improvement, we show that ps excitation allows for both CARS imaging with high spectral resolution and TPEF and SHG imaging with good sensitivity. This method is not only suitable for ps-ps CARS, but also applicable for fs-fs CARS, fs TPEF, three-photon fluorescence, and third harmonic generation. According to theory, this pulse-picking technology gives better sensitivity enhancement for higher-order nonlinear optical processes.

Methods

Mia PaCa-2 cell culture

Mia PaCa-2 pancreatic cancer cells (ATCC) were cultured in Dulbecco's Modified Eagle Medium (DMEM, ATCC) with 10% fetal bovine serum (FBS, ATCC) and 1% penicillin/streptomycin. The cells were seeded in glass-bottom dishes (MatTek Life Sciences) with 2 mL culture medium and cultured in a CO₂ incubator set to 37 °C

with a 5% CO₂ concentration. Cells were grown to 50-60% confluency and were directly used for live-cell imaging or fixed with 10% buffered formalin phosphate (Fisher Chemical) for imaging.

Fluorescence labeling of mitochondria

Mia PaCa-2 cells were stained with MitoView 405 (Biotium). Cells were first allowed to attach to a glass-bottom dish and then incubated with a 100 nM solution of MitoView for 15 minutes at 37 °C before imaging. The MitoView stock solution was prepared in DMSO at 100 μM.

Mouse tissue preparation

Organs from wild-type mice were surgically removed and then preserved in 10% buffered formalin phosphate (Fisher Chemical) and stored in a 4 °C refrigerator. Tissue samples (liver, kidney, brain, and tail tendon) were sliced and sandwiched between two glass slides for imaging.

Chemical sample preparation

Samples of pure methanol (Sigma-Aldrich), dimethyl sulfoxide (DMSO, Fisher Chemical), and DMSO in D₂O (Sigma-Aldrich) for imaging were prepared by sandwiching a drop of each between two thin glass coverslips with double-sided tape as the spacer. For sensitivity measurements, a 50% (v/v) sample of DMSO/D₂O was prepared and serially diluted to the desired % concentration. Fluorescent (2104 Green polystyrene, ex 450/ em 500), PMMA (Catalog# MMA1000), and PS microparticles (Catalog# 112), all 1 μm in size, were obtained from Degradex by Phosphorex, mixed if necessary, and deposited between glass coverslips for imaging.

Pulse-picking CARS imaging

The optical design and working principle of the PPCARS microscope are illustrated in Fig. 1. A dual-output 80-MHz femtosecond pulsed laser source (InSight X3+, Spectra-Physics) was used for signal excitation. The 120-fs wavelength tunable output (680-1300 nm) was used as the pump beam and the 120-fs 1045 nm fixed-wavelength output was used as the Stokes beam. The beams were chirped using glass rods (SF57, Lattice Electro Optics). One 150 mm rod was placed in the probe beam pathway and two 150 mm rods were used to chirp the combined beams. We bent the optical beams to double-pass the two chirping rods to increase the chirping. This 1+4 (Stokes + combined) configuration allows us to chip the pump beam to 3.4 ps and the Stokes beam to 1.8 ps before entering the microscope. Hyperspectral CARS imaging was performed by scanning a 1D motorized delay stage (X-LSM050A, Zaber Technologies) at 10 μm per step while collecting single-colour CARS images at each delay position. The combined beams were then directed to an acousto-optic modulator (1250-C, Isomet) and modulated at different frequencies by a function generator (DG1022Z, Rigol). The modulated 1st order beams were directed to a 2D galvo scanner set (GVS002, Thorlabs) and then into an upright microscope (Olympus BX51). Either a 40x/0.8 NA (LUMPLFLN 40XW, Olympus) or a 60x/1.2 NA water immersion objective lens (UPLSAPO 60X, Olympus) was used to focus the beams onto the sample. The FCARS signal was collected by a 1.4 NA oil-immersion condenser. For FCARS imaging in the C-H region, the signal was

directed through a 776 long-pass dichroic mirror (FF776-Di01-25x36, Semrock) and then detected with a PMT (H7422P-40, Hamamatsu) combined with a PMT amplifier (PMT-4V3 amplifier, Advanced Research Instruments Corp). For FCARS imaging in the fingerprint region, a combination of filters was used before a modified PMT (PMT1001, Thorlabs) for signal acquisition, and the signals were also amplified by the PMT-4V3 amplifier. For epi-imaging, the signals were directed using a 776 nm long-pass dichroic mirror (FF776-Di01-25x36, Semrock), separated using a 538 nm long-pass dichroic mirror (FF536-FDi01-25x36, Semrock), and then detected with separate PMT. For the FCARS and ECARS detections, 655/30 nm filters were used (AT655/30m, Chroma Technology). For epi-detected TPEF, two separate channels, including PMT2 with a 451/106 nm filter (FF01-451/106-25, Semrock) and PMT3 with a 575/59 nm filter (FF01-575/59-25, Semrock) were used to detect fluorescence signals in different ranges. We used only 800 nm pulses to excite the fluorescence beads, and both 800 nm and 1045 nm pulses for tissue imaging. For SHG signal detection, a 520/20 nm filter was used with PMT3. A 3D motorized translational stage (H101, ProScan III, Prior Technology) was used to control sample and objective positions and perform automated large-area image acquisition and stitching, as well as 3D imaging.

Image acquisition and analysis

All images were acquired by a data acquisition card (PCIe-6363, National Instruments) and lab-written software based on LabVIEW. The original images were saved in .txt format and processed by ImageJ. Image contrast and brightness were adjusted for proper display. Pseudo-colour maps were also created by ImageJ functions. Intensity profiles were analyzed by ImageJ and plotted using Origin. Spectral phasor analysis was performed by a phasor plug-in reported in previous publications [29]. Gates for different compositions were manually selected for chemical separations. For SNR analysis, signals were selected from the sample areas and noises were chosen from the blank locations. For sensitivity analysis, to avoid PMT saturation, we use different input powers for different duty cycles (Table S1, Figure S1). The intensities were calibrated using the pump and Stokes power values. The SNR increases shown in Fig. 1 and Figure S2 were derived by dividing the calibrated SNR at each duty cycle by the SNR from the 97% duty cycle. We used a 97% duty cycle to mimic normal CARS imaging conditions since the function generator cannot generate 100% duty cycle square waves. TPEF and SHG SNR increases were analyzed similarly. Large-area mapping images were acquired on a separate software written in LabVIEW to control the 2D translational sample stage for automated image stitching. 3D image acquisition was also performed using a lab-written LabVIEW program.

Phase retrieval of CARS spectra

Phase retrieval was performed using a lab-written MATLAB script. This script is based on Kramers–Kronig relations and is utilized for removing the nonresonant background and obtaining Raman spectra from the hyperspectral CARS imaging of DMSO in D₂O below 1% concentration, mixed PMMA and PS beads, and MIA PaCa-2 cells.

Declarations

Acknowledgment

We want to thank Judy Hallett at Purdue University Bindley Bioscience Center for sharing the mouse carcass for tissue harvest. We also want to thank Dr. Garth Simpson for sharing the autocorrelator and compact power metre for the measurement of pulse width and power at the sample. This research is supported by the Purdue University Department of Chemistry startup fund to C.Z.

Author contributions

C.Z. designed the project. M.C. and C.Z. designed and performed the experiments. M.C. and C.Z. analyzed the data. G.G. prepared cell and tissue samples. M.C. and C.Z. wrote the paper.

Competing Interests statement

The authors declare no competing interests.

Ethics statement

The present study used mouse samples from the Purdue University Center for Cancer Research's Transgenic and Genome Editing Facility. The use of mice was approved by the Purdue Institutional Animal Care and Use Committee (protocol 1111000211).

References

1. Evans, C.L. and X.S. Xie, *Coherent anti-Stokes Raman scattering microscopy: chemical imaging for biology and medicine*. *Annu. Rev. Anal. Chem.*, 2008. **1**: p. 883–909.
2. Min, W., et al., *Coherent nonlinear optical imaging: beyond fluorescence microscopy*. *Annual Review of Physical Chemistry*, 2011. **62**: p. 507–530.
3. Chung, C.-Y.J. and E.O. Potma, *Biomolecular imaging with coherent nonlinear vibrational microscopy*. *Annual Review of Physical Chemistry*, 2013. **64**: p. 77–99.
4. Cheng, J.-X. and X.S. Xie, *Vibrational spectroscopic imaging of living systems: An emerging platform for biology and medicine*. *Science*, 2015. **350**(6264).
5. Zumbusch, A., G.R. Holtom, and X.S. Xie, *Three-dimensional vibrational imaging by coherent anti-Stokes Raman scattering*. *Physical Review Letters*, 1999. **82**(20): p. 4142.
6. Cheng, J.-X. and X.S. Xie, *Coherent anti-Stokes Raman scattering microscopy: instrumentation, theory, and applications*. *Journal of Physical Chemistry B*, 2004. **108**(3): p. 827–840.
7. Evans, C.L., et al., *Chemical imaging of tissue in vivo with video-rate coherent anti-Stokes Raman scattering microscopy*. *Proceedings of the National Academy of Sciences, U.S.A*, 2005. **102**(46): p. 16807–16812.
8. Freudiger, C.W., et al., *Label-free biomedical imaging with high sensitivity by stimulated Raman scattering microscopy*. *Science*, 2008. **322**(5909): p. 1857–1861.
9. Zhang, D., M.N. Slipchenko, and J.-X. Cheng, *Highly sensitive vibrational imaging by femtosecond pulse stimulated Raman loss*. *Journal of Physical Chemistry Letters*, 2011. **2**(11): p. 1248–1253.
10. Ji, M., et al., *Rapid, label-free detection of brain tumors with stimulated Raman scattering microscopy*. *Science Translational Medicine*, 2013. **5**(201): p. 201ra119-201ra119.

11. Camp Jr, C.H., et al., *High-speed coherent Raman fingerprint imaging of biological tissues*. Nature Photonics, 2014. **8**(8): p. 627–634.
12. Freudiger, C.W., et al., *Stimulated Raman scattering microscopy with a robust fibre laser source*. Nature Photonics, 2014. **8**(2): p. 153–159.
13. Zhang, C., D. Zhang, and J.-X. Cheng, *Coherent Raman scattering microscopy in biology and medicine*. Annual review of biomedical engineering, 2015. **17**: p. 415–445.
14. Gong, L., et al., *Higher-order coherent anti-Stokes Raman scattering microscopy realizes label-free super-resolution vibrational imaging*. Nature Photonics, 2020. **14**(2): p. 115–122.
15. Steuwe, C., et al., *Surface enhanced coherent anti-Stokes Raman scattering on nanostructured gold surfaces*. Nano Letters, 2011. **11**(12): p. 5339–5343.
16. Fast, A., et al., *Surface-enhanced coherent anti-Stokes Raman imaging of lipids*. Applied Optics, 2016. **55**(22): p. 5994–6000.
17. Filipczak, P., et al., *Spontaneous versus Stimulated Surface-Enhanced Raman Scattering of Liquid Water*. Journal of Physical Chemistry C, 2020. **125**(3): p. 1999–2004.
18. Zong, C., et al., *Plasmon-enhanced stimulated Raman scattering microscopy with single-molecule detection sensitivity*. Nature Communications, 2019. **10**(1): p. 1–11.
19. Wei, L., et al., *Super-multiplex vibrational imaging*. Nature, 2017. **544**(7651): p. 465–470.
20. Tian, S., et al., *Polydiacetylene-based ultrastrong bioorthogonal Raman probes for targeted live-cell Raman imaging*. Nature Communications, 2020. **11**(1): p. 1–9.
21. Zhuge, M., et al., *Ultrasensitive Vibrational Imaging of Retinoids by Visible Preresonance Stimulated Raman Scattering Microscopy*. Advanced Science, 2021. **8**(9): p. 2003136.
22. Xiong, H., et al., *Stimulated Raman excited fluorescence spectroscopy of visible dyes*. Journal of Physical Chemistry Letters, 2019. **10**(13): p. 3563–3570.
23. Xiong, H., et al., *Stimulated Raman excited fluorescence spectroscopy and imaging*. Nature Photonics, 2019. **13**(6): p. 412–417.
24. Bi, Y., et al., *Near-resonance enhanced label-free stimulated Raman scattering microscopy with spatial resolution near 130 nm*. Light: Science & Applications, 2018. **7**(1): p. 1–10.
25. Liao, C.-S., et al., *Denoising stimulated Raman spectroscopic images by total variation minimization*. Journal of Physical Chemistry C, 2015. **119**(33): p. 19397–19403.
26. Manifold, B., et al., *Denoising of stimulated Raman scattering microscopy images via deep learning*. Biomedical Optics Express, 2019. **10**(8): p. 3860–3874.
27. Yamato, N., et al., *Improvement of nerve imaging speed with coherent anti-Stokes Raman scattering rigid endoscope using deep-learning noise reduction*. Scientific Reports, 2020. **10**(1): p. 1–11.
28. Qian, C., et al., *Super-resolution label-free volumetric vibrational imaging*. Nature Communications, 2021. **12**(1): p. 1–10.
29. Fu, D., et al., *Hyperspectral imaging with stimulated Raman scattering by chirped femtosecond lasers*. Journal of Physical Chemistry B, 2013. **117**(16): p. 4634–4640.
30. Vartiainen, E.M., *Phase retrieval approach for coherent anti-Stokes Raman scattering spectrum analysis*. Journal of the Optical Society of America B, 1992. **9**(8): p. 1209–1214.

31. Liu, Y., Y.J. Lee, and M.T. Cicerone, *Broadband CARS spectral phase retrieval using a time-domain Kramers–Kronig transform*. Optics Letters, 2009. **34**(9): p. 1363–1365.
32. Hong, W., et al., *In situ detection of a single bacterium in complex environment by hyperspectral CARS imaging*. ChemistrySelect, 2016. **1**(3): p. 513–517.
33. Huang, K.-C., et al., *Multiplex stimulated Raman scattering imaging cytometry reveals lipid-rich protrusions in cancer cells under stress condition*. iScience, 2020. **23**(3): p. 100953.
34. Schwille, P., et al., *Molecular dynamics in living cells observed by fluorescence correlation spectroscopy with one-and two-photon excitation*. Biophysical Journal, 1999. **77**(4): p. 2251–2265.
35. Tu, H., et al., *Stain-free histopathology by programmable supercontinuum pulses*. Nature Photonics, 2016. **10**(8): p. 534–540.

Figures

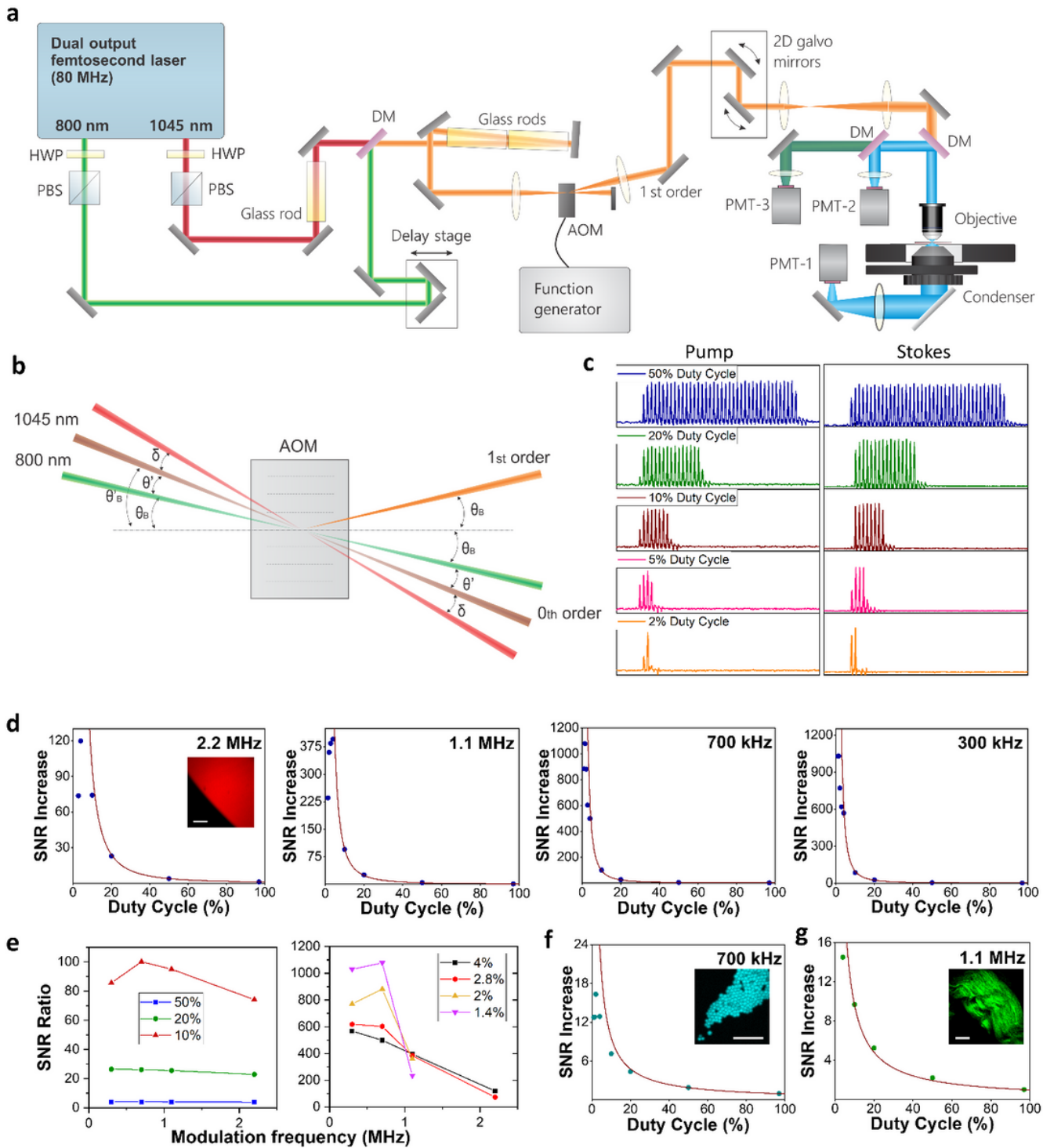


Figure 1

Pulse-picking technology for sensitivity improvement of CARS, TPEF, and SHG modalities. (a) Schematic of the PPCARS microscope configuration. PBS, polarization beam splitter; AOM, acousto-optic modulator; PMT, photomultiplier tube; DM, dichroic mirror; HWP, half-wave plate. (b) Schematic of spatial overlapping of pump and Stokes beams at the 1st order diffraction of an AOM. (c) Pump and Stokes pulse trains from the AOM 1st order beam at 50%, 20%, 10%, 5%, and 2% duty cycles. (d) CARS SNR increases versus duty cycle at 2.2, 1.1, 0.7, and 0.3 MHz modulation frequencies. Dots are experimental data, curves are the theoretical function of $1/D^2$, D is the duty cycle. The image inset shows a CARS image of DMSO edge from which SNR values were derived. (e)

CARS SNR increases versus modulation frequency at different duty cycles. (f) TPEF SNR increases versus duty cycle at 700 kHz modulation frequency. Dots are experimental data, the curve is the theoretical function of $1/D$. The image inset shows fluorescent microparticles from which SNR values were derived. (g) SHG SNR increases versus duty cycle at 1.1 MHz modulation frequency. Dots are experimental data, the curve is the theoretical function of $1/D$. The image inset shows a mouse tail tendon specimen from which SNR values were derived. Scale bars, 10 μm .

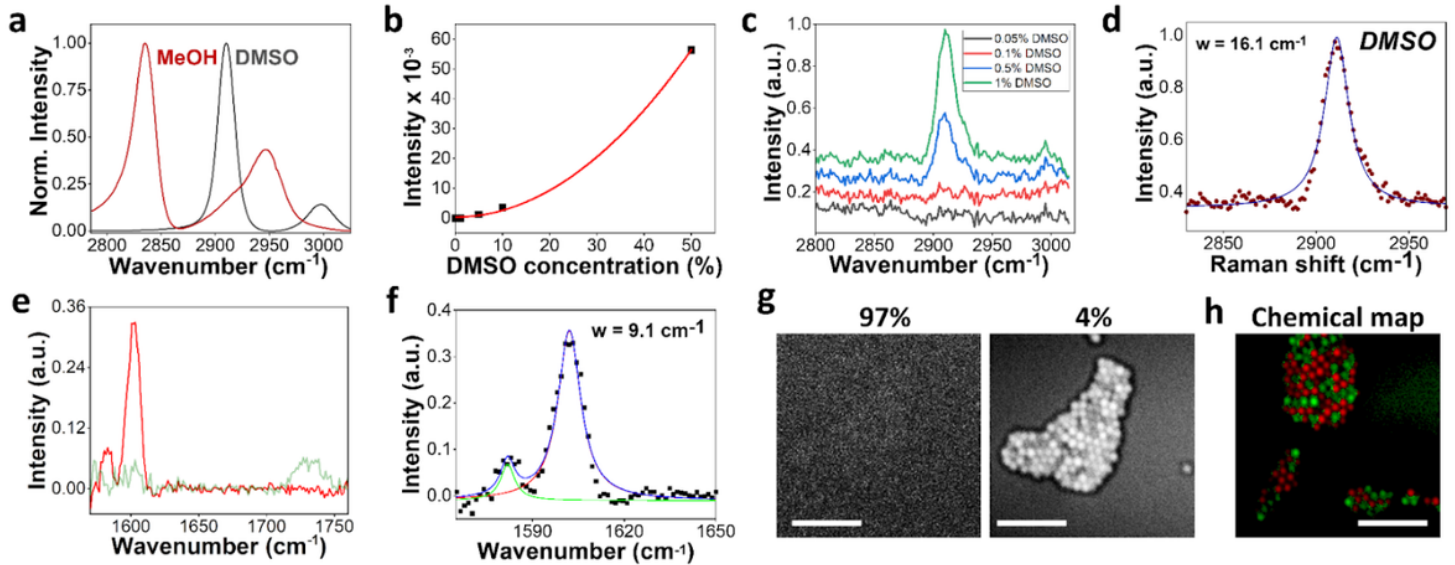


Figure 2

Characterizations of the PPCARS microscope. (a) CARS spectra of methanol and DMSO in the C-H region. (b) A plot of CARS signal intensity versus DMSO concentration (%) in D2O. Dots are experimental values, the curve is the quadratic fitting of experimental results. (c) Phase-retrieved Raman spectra of 1%-0.05% DMSO in D2O. (d) Peak fitting of phase-retrieved Raman spectrum of 1% DMSO in D2O. (e) Fingerprint region retrieved Raman spectra of 1 μm PS (red) and PMMA beads (green) from PPCARS images. (f) Spectral peak fitting of PS 1583 cm^{-1} and 1602 cm^{-1} stretching. (g) CARS images of a mixture of 1 μm PS and PMMA beads at 97% and 4% duty cycles, 700 kHz modulation frequency. (h) Spectral-phasor-generated chemical map of mixed beads (PS: red; PMMA: green) using the fingerprint hyperspectral PPCARS images. Power at the samples: 5.2 mW pump and 6.2 mW Stokes for the C-H imaging; 13.7 mW pump and 6.2 mW Stokes for the fingerprint imaging. Scale bars, 10 μm .

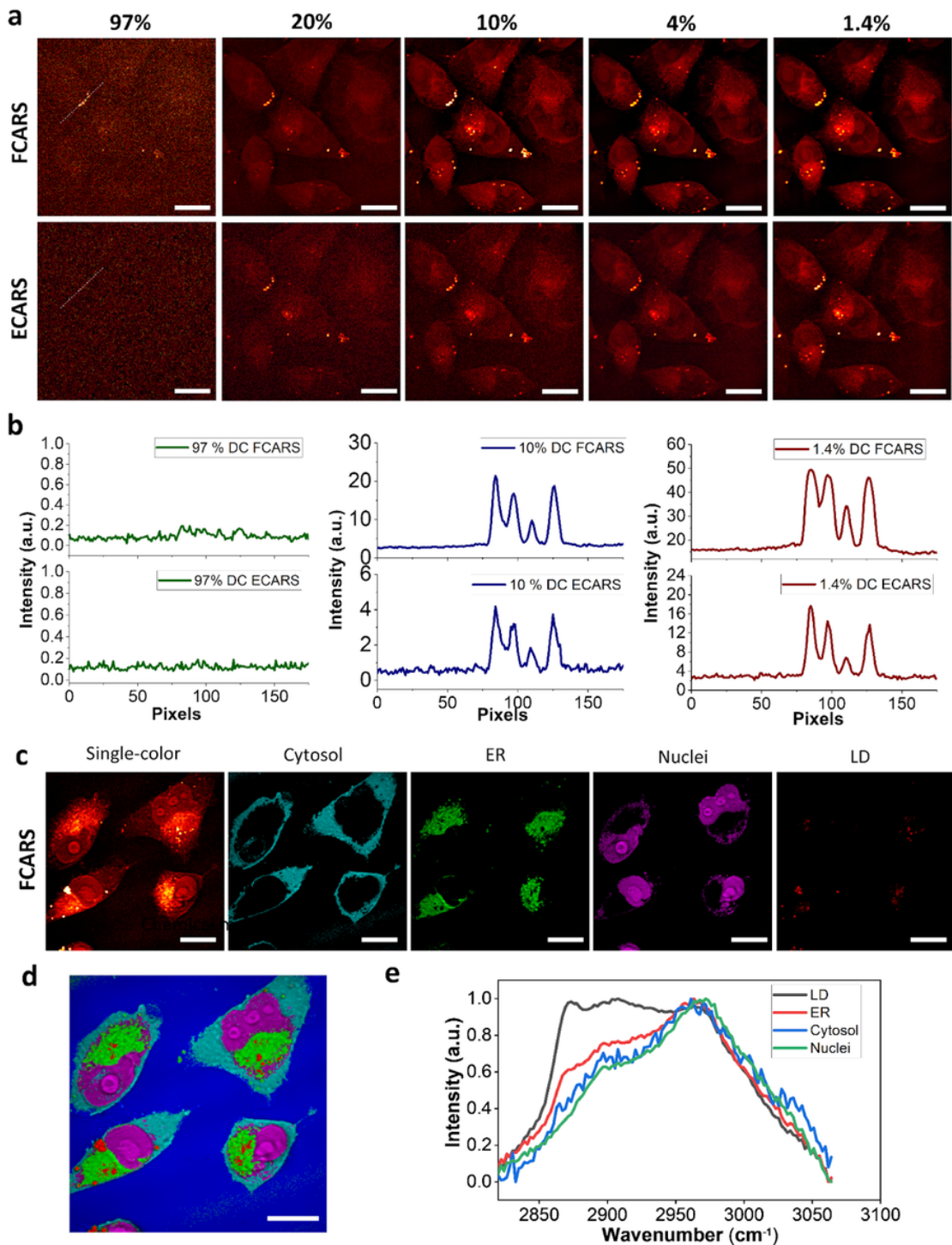


Figure 3

PPCARS imaging and chemical segmentation of cells. (a) FCARS (top) and ECARS (bottom) images of Mia PaCa-2 cells at 97%, 20%, 10%, 4%, and 1.4% duty cycles at 700 kHz modulation frequency. (b) Line profile plots for FCARS (top) or ECARS (bottom) images at 97%, 10%, and 1.4% duty cycles along the lines in panel a. (c) Single-colour CARS and spectral unmixing images for Mia PaCa-2 cells. ER, endoplasmic reticulum; LD, lipid droplets. (d) A chemical map of Mia PaCa-2 cells composed of the cytosol, ER, nuclei, and LD compositions. (e) Phase-retrieved Raman spectra from four cellular components. Power at the samples for all images: pump 2.0 mW, Stokes 3.7 mW, pixel dwell time 10 μ s. Scale bars, 10 μ m.

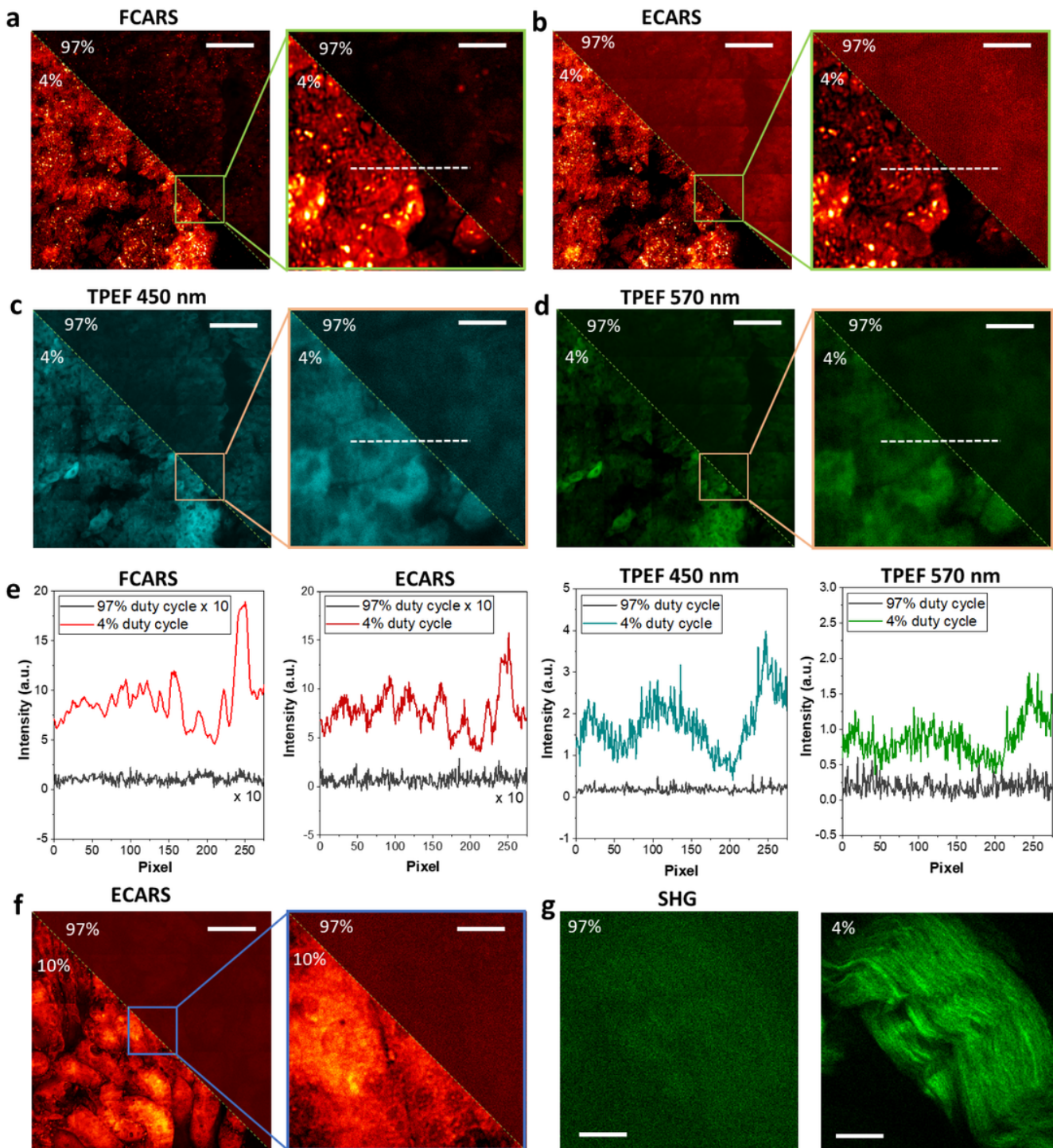


Figure 4

Multimodal imaging of mouse tissue samples at high and low duty cycles. (a-d) Side-by-side comparison of 4% and 97% duty cycles for FCARS (a), ECARS (b), TPEF 450 nm (c), and TPEF 570 nm (d) imaging of a mouse liver sample (left) and the magnified selected region (right). (e) Line profile plots along the dashed line selected in panels (a-d) for four imaging modalities. Gray, 97% duty cycle. Colour-coded, 4% duty cycle. The 97% line profiles for FCARS and ECARS are multiplied by 10. (f) Side-by-side comparison of 10% and 97% duty cycles for ECARS imaging of a mouse kidney sample (left) and the magnified selected region (right). (g) Comparison of 97% and 4% duty cycles for SHG imaging of mouse tail tendon. Power at the samples: pump 18.0 mW, Stokes

12.6 mW for CARS and TPEF; 1.4 mW 1045 nm for SHG. Pixel dwell time: 10 μ s. Scale bars, 50 μ m and 10 μ m for left and right images, respectively, for each panel.

Supplementary Files

This is a list of supplementary files associated with this preprint. Click to download.

- [SupplementaryInformationV3.docx](#)
- [SupplimentaryVideo1.avi](#)